Analytical Methods

PAPER

View Article Online
View Journal | View Issue

Cite this: *Anal. Methods*, 2017, **9**, 6653

Simultaneous determination of sulfur isotopes and trace elements in pyrite with a NanoSIMS 50L†

Jianchao Zhang,[ab] Yangting Lin,*[ab] Jun Yan,[c] Jinxiang Li[c] and Wei Yang[ab]

Pyrite is common sulfide mineral involved in the formation of various ores and hydrothermal and biogenetic activities, and its S isotopic ratios and trace element contents and their spatial distribution have been recorded in the processes of these events. We established simultaneous analyses of $^{34}S/^{32}S$ ratios and trace element contents of pyrite using nanometer-scale secondary ion mass spectrometry (NanoSIMS). Firstly, the images of S ($^{34}S^-$), As ($^{75}As^-$), Se ($^{80}Se^-$), Cu ($^{63}Cu^{32}S^-$), Au ($^{197}Au^-$) and Pb ($^{208}Pb^{32}S^-$) of pyrite were acquired by rastering areas ranging from 20 × 20 μm^2 to 40 × 40 μm^2 using a Cs^+ beam of 7–10 pA with a diameter of ~250 nm. Then, the $^{34}S/^{32}S$ ratios ($^{32}S^-$ measured by using a Faraday cup and $^{34}S^-$ measured by using an electron multiplier) and the concentrations of these trace elements of the individual layers of the zoned pyrite grains were simultaneously measured in spot analysis mode, by rastering the same current over an area of 2 × 2 μm^2. The $^{34}S/^{32}S$ ratios were calibrated for matrix effects with pyrite standard Balmat or Py1117, and the external reproducibility (1SD) is <0.5‰. The concentrations of trace elements were calibrated using the relative sensitivity factors (RSFs) of As, Se, Cu, Au and Pb, which were determined from pyrite grains with zoning layers. The determined RSFs of As, CuS, Au and PbS are 4.43 ± 0.28, 0.36 ± 0.04, 0.18 ± 0.03 and 38.0 ± 15.1, respectively. Pyrite from Lannigou Carlin type gold deposits was analyzed as an example, and the results revealed three main episodes of its formation, with each superposed by micron-width oscillation zonings of trace elements. This method has important potential applications in isotopic and elemental investigation of thin layers of pyrite and other sulfides.

Received 9th June 2017
Accepted 27th October 2017

DOI: 10.1039/c7ay01440f

rsc.li/methods

1. Introduction

Pyrite is the most common sulfide mineral, and the sulfur isotope ratio and trace elements are important indicators to trace sulfur reservoirs, reveal the formation of ore deposits and figure out the geochemical process.[1–5] In particular, isotopic and elemental investigation of very thin zoning layers (1–5 μm) which are commonly observed in pyrite grains is significant to distinguish the different ore-stages and to uncover the compositional evolution of the parent hydrothermal fluid.[6–10] Sulfur isotope or trace element distribution in the zoned pyrite grains has been reported in the literature, using laser ablation inductively coupled plasma mass spectrometry (LA-ICP-MS)[11–15] and secondary ion mass spectrometry (SIMS).[9,16–23] Compared with LA-ICP-MS, traditional SIMS (CAMECA IMS f series and 1270/1280(HR) instruments) has a higher lateral resolution of typically 10–30 μm in size. To improve the lateral resolution, Williford *et al.* (2011) performed high precision analyses of sulfur isotopes on an IMS 1280 with 3 × 2 μm spots and achieved a precision of 0.82‰ (2SD) with two Faraday cups for detection.[24] The aim of this study was to perform sulfur isotope analyses with high precision and high lateral resolution, combined with trace element measurements, which is required in the analyses of complexly zoned pyrite grains with thin layers of 1–3 μm in width (*e.g.* typical thin rims of pyrite in Carlin-type deposits).[8,25–28] Due to the sector geometry of magnetic fields, traditional SIMS does not allow the simultaneous analysis of sulfur isotopes and trace elements in the same zoning layers, which imposes constraints on the mineral formation.

The CAMECA NanoSIMS 50L has the unique advantage of extremely high lateral resolution, up to 50 nm for a Cs^+ beam and a large mass range of multicollection because of its Mattauch–Herzog geometry. It is the most promising tool to achieve simultaneous analyses of sulfur isotopes and trace elements in thin zoning layers with the width of 1–3 μm. A typical precision for sulfur isotopes achieved by NanoSIMS was about 2–3‰,[29–31] and recently improved to ~0.5‰ (1SD) at a high lateral resolution of ~2 μm.[24,32] A primary ion beam of cesium was normally used to perform sulfur isotope measurements because of its high ion yield. Normally, trace elements have very low ion yields under the sputtering of Cs^+.[33] However, Storms *et al.* (1977) reported that the ion yield of noble metals (Au, Pt and Ir) under a Cs^+ source was higher than that under an O^- source.[34] It was

[a]*Key Laboratory of Earth and Planetary Physics, Institute of Geology and Geophysics, Chinese Academy of Sciences, Beijing 100029, China. E-mail: LinYT@mail.iggcas.ac.cn*
[b]*Institutions of Earth Science, Chinese Academy of Sciences, Beijing 100029, China*
[c]*Key Laboratory of Ore Deposit Geochemistry, Institute of Geochemistry, Chinese Academy of Sciences, Guiyang 550002, China*

† Electronic supplementary information (ESI) available. See DOI: 10.1039/c7ay01440f

also reported by Hsu *et al.* (2000) that a Cs^+ beam was used to measure the abundances of Os, Ir, Au, Pt, Ni and Co in the Fe–Ni metals of iron meteorites.[35] Barker *et al.* (2009) utilized the ion species of CuS, AsS and FeS to improve the detection limit for Cu, As and Fe in sulfides. Also, they developed imaging analyses of sulfur isotopes together with As, Au, Cu, and Te with NanoSIMS, which revealed variations in S isotopic ratios and the trace elements within the grains of Carlin-type pyrite.[8] The work of Barker *et al.* (2009) mainly focused on the zoning patterns of trace elements and sulfur isotopes. They only obtained the relative variabilities of S isotope ratios and trace element contents in the zoning patterns without accurately quantifying them using calibration standards.

In this study, we developed high precision quantitative analyses of sulfur isotope and trace element contents together with high spatial resolution images of trace elements in complexly zoned pyrite with NanoSIMS. Secondary ion images with high lateral resolution were obtained to reveal the zoning patterns and growth stage within the pyrite grains. To ensure the analytical accuracy, sulfur isotope ratios were calibrated with instrumental mass fractionation by a standard–sample–standard bracket method using the standards measured together with the samples. To obtain the relative sensitivity factors (RSFs) of trace elements, layers enriched with trace elements in Carlin-type pyrite were measured with both EPMA and NanoSIMS at exactly the same spot.

2. Sample description

Three natural pyrite standards, Balmat pyrite, PY1117 and CS01, were utilized as the references for sulfur isotopes. The standards and samples were embedded in epoxy resin and made into polished disks with a diameter of 10 mm and 25.4 mm, respectively. Another 10 mm polished disk with arsenopyrite, $FeSe_2$, chalcopyrite, gold foil, and galena embedded in epoxy was used to determine the mass peak location and to check possible isobaric interference. The Au foil was impressed into an indium disk with a diameter of 12.7 mm. All of the standard, sample and reference disks were coated with carbon and mounted on the same geo-sample holder which can hold five sample disks, including one sample disk with a diameter of 25.4 mm, two with a diameter of 12.7 mm and two with a diameter of 10 mm.

2.1 Standards for sulfur isotope analyses

Balmat pyrite is a widely used standard of sulfur isotopes. However, a range of $\delta^{34}S_{VCDT}$ values have been reported, varying from (1SD) 15.1 ± 0.2‰ to 16.5 ± 0.3‰.[17,19–21,36] The Balmat pyrite measured in this study was supplied by S. J. Mojzsis who reported a $\delta^{34}S_{VCDT}$ of 16.5 ± 0.3‰ (1SD) in 2003 and 16.3 ± 0.3‰ (1SD) in 2005.[20,21] The value of the new Balmat was confirmed by Ushikubo *et al.* (2014) with a stable mass spectrometer ($\delta^{34}S_{VCDT} = 16.04 \pm 0.2‰$).[19,37] PY-1117 was from pyrite veins (2–4 mm wide) at a depth of 62 m in Qulong, Tibet, China.[38] CS01 was separated from a massive pyrite–pyrrhotite gold bearing ore from the Chaoshan gold deposit, Eastern Yangtze Craton, Eastern China.[39] Both pyrites have homogeneous sulfur isotopic compositions, and their $\delta^{34}S_{VCDT}$ values were determined by using a stable isotope mass spectrometer (Thermo Finnigan Delta-S), 0.3 ± 0.1‰ for PY-1117 and 4.6 ± 0.2‰ for CS01.[32] They were used as the working references for sulfur isotope analyses in this study. These standards cannot be utilized to perform trace element measurements. Trace elements (Au, As, Cu, *etc.*) in Balmat and 1117 were very poor. Balmat was reported to have <10 ppm of Ag, <100 ppm of Cu and several hundred ppm of Pb as trace elements.[40] The pyrite grains were also highly heterogeneous in trace elements.

2.2 Samples

The pyrite grains from Lannigou Carlin type gold deposits were analyzed to determine the relative sensitivity factors (RSFs) of trace elements in this study. The deposit is located at the northeastern corner of the Lanzishan Dome within the Yunnan–Guizhou–Guangxi "golden triangle" area.[41–43] These pyrite grains were characterized as a high-grade Carlin-type with the size mainly ranging from 40–100 μm. Gold mainly occurs in arsenic-rich rims with the width of 2–5 μm. The samples were sectioned and polished for optical microscopy observation, and backscattered electron imaging by scanning electron microscopy. Then the content of trace elements in arsenic-rich rims was measured by using an electron microprobe and NanoSIMS to calculate the RSFs.

3. Analytical method

3.1 NanoSIMS analysis

Trace element mapping and the subsequent quantitative analysis of sulfur isotope ratios and trace element contents of pyrite were performed with a CAMECA NanoSIMS 50L instrument at the Institute of Geology and Geophysics, Chinese Academy of Sciences. In previous studies with NanoSIMS, sulfur isotopes were counted with electron multipliers (EMs) with a small Cs^+ beam current for the highest lateral resolution. However the accuracy of analysis was significantly affected by quasi-simultaneous arrival (QSA) effects.[31,44,45] Due to QSA effects, the counting efficiency for ^{32}S was affected by 70–100‰ and it will be only 3–4‰ for ^{34}S.[32,45] To avoid the QSA effect on ^{32}S and improve the analytical accuracy, $^{32}S^-$ was counted with Faraday cups and $^{34}S^-$ with an EM using a Cs^+ beam current of 7 pA and a diameter of ~250 nm. According to the definition of the QSA effect[45] it results in a bias of the counting efficiency for ^{34}S and the ratio of $^{34}S/^{32}S$ by 3–4‰. And the bias depends on the secondary ion yield (K) of ^{34}S which was the counting rate normalized by primary beam intensity. If the ion yield (K) was constant, the bias could be eliminated by using matrix-matched standards. It was observed that the ion yield varied by less than 3%. According to the calculation,[32,45] QSA effects would introduce an additional error within ~0.1‰ which could be neglected, compared with analytical precision. EM aging by $^{34}S^-$ with a counting rate of 2–2.5 × 10^5 was monitored every 4 hours. Besides, secondary ions of $^{34}S^-$, $^{75}As^-$ ($^{715}As^{32}S^-$), $^{80}Se^-$, $^{63}Cu^{32}S^-$, $^{197}Au^-$ and $^{208}Pb^{32}S^-$ were simultaneously

detected with EMs in the multi-collection mode (Fig. 1). The mass peak positions of $^{75}As^-$ ($^{75}As^{32}S^-$), $^{80}Se^-$, $^{63}Cu^{32}S^-$, $^{197}Au^-$ and $^{208}Pb^{32}S^-$ were confirmed by the working references of arsenopyrite, $FeSe_2$, chalcopyrite, Au foil and galena, respectively (Fig. 2). In the first session, ^{75}As was measured in the analysis. Then it was found that $^{75}As^{32}S^-$ has a much higher ion yield which was about 30 times higher than that of $^{75}As^-$. We measured $^{75}As^{32}S^-$ in the following sessions. In the paper, As^- was used to calculate the relative sensitivity factor. The ratio of $^{75}As^-/^{75}As^{32}S^-$ was constant with a value of 0.03 (Fig. 3), and therefore, when AsS^- was measured in the following sessions, $^{75}As^{32}S^-/^{32}S$ could be converted to $^{75}As/^{32}S$ according to the factor of ~0.03. A mass resolution of ~3000 ($M/\Delta M$ measured at 10% peak height) was achieved using the width of the entrance slit (30 μm), aperture slit (200 μm) and exit slit (90 μm), which is enough to eliminate the isobaric interference of $^{32}SH_2^-$ and $^{33}SH^-$ on $^{34}S^-$, $^{56}FeC_2^-$ and $^{32}S_2{}^{16}O^-$ on $^{80}Se^-$, $^{54}Fe_2{}^{57}Fe^{32}S^-$ and $^{32}S_4{}^{34}S_2H^-$ on Au^-, and $^{56}Fe_2{}^{32}S_4^-$ on $^{208}Pb^{32}S^-$. There is an irregular step-like feature shown at the right side of the mass spectrum of $^{75}As^{32}S$. The mass difference between isobaric interference and $^{75}As^{32}S$ was ~0.0012 (Fig. S1†). To identify the species of isobaric interference, the secondary ion images of ^{34}S, $^{75}As^{32}S$, ^{16}O, and ^{12}C and isobaric interference were obtained and are shown in the ESI (Fig. S1†). The isobaric interference mainly existed in some hotspots which were also enriched with O and C, but lack S and As. These hotspots of isobaric interference were normally regarded as inclusions or holes. We usually avoid these areas in the analysis. Therefore, the interference has no influence on the measurement of AsS. It was noticed that the mass peak of $^{208}Pb^{32}S^-$ failed to be resolved from $^{206}Pb^{34}S^-$ and $^{207}Pb^{33}S^-$; however their contributions could be neglected because of the low relative abundances of $^{206}Pb^{34}S^-$ and $^{207}Pb^{33}S^-$ (<4%).

The area of interest was first pre-sputtered with a high primary beam of ~1 nA, in order to remove the carbon coating and to stabilize the secondary ion yield. The area ranging from 20 × 20 to 40 × 40 μm^2 was then mapped using a low beam current of 7–10 pA with a diameter of 250 nm, and the data were accumulated as images with a pixel resolution of 256 × 256 or 512 × 512 for the secondary ions including $^{34}S^-$, $^{75}As^-$, $^{80}Se^-$, $^{63}Cu^{32}S^-$, $^{197}Au^-$ and $^{208}Pb^{32}S^-$, except for $^{32}S^-$ which was counted with Faraday cups. Each image contained 3 frames, and the total analysis time was ~30 min. Individual frames were added together after correction for position shift, using the WinImage software (CAMECA). According to the elemental image, several 2 × 2 μm^2 sized areas of interest were selected and the simultaneous sulfur isotope ($^{34}S/^{32}S$) and trace element ($A/^{32}S$, A = As, CuS, Se, Au, PbS) analyses were performed (5–8 min for each area). The sulfur isotopic ratio was corrected for dead-time with instrumental mass fractionation (IMF).

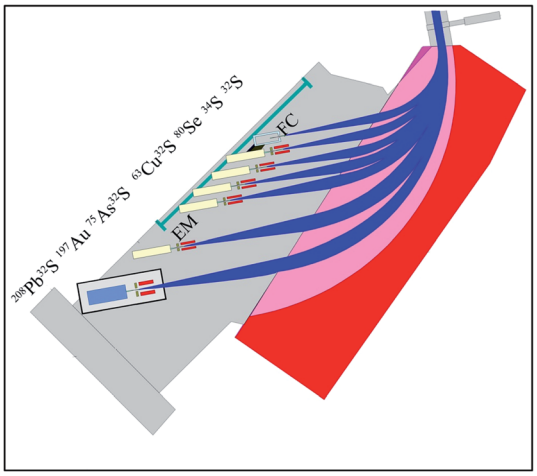

Fig. 1 The configuration of multi-collection in this study.

3.2 Electron probe microanalysis

To determine the relative sensitivity factors of the trace elements, electron probe microanalysis (EPMA) was carried out using a JEOL JXA-8100 at the College of Earth Sciences & Land Resources, Chang'an University. The area mapped by NanoSIMS was also characterized using backscattered electron scanning microscopy (BSE). After zoning layer recognition in the elemental image and BSE image, major elements (Fe, S and As) were measured using an electron beam with a diameter of ~2 μm at 15 keV energy and 10 nA current; after the measurements of Fe, S and As, trace elements of Au, Ni, Co, Cu, Se and Pb were measured in the same spot positions with a much higher beam current of 100 nA. The detection limits of the trace elements were between 100 and 200 ppm. The uncertainty ranged from 2 to 5% for As, 30 to 50% for Au, and from 10 to 30% for Cu and Pb.

4. Results and discussion

This analytical method provides elemental images, trace element contents and sulfur isotope ratios in exactly the same zoning layers of pyrite grains. Elemental images were obtained by NanoSIMS before the spot analysis, which clearly show the trace element distribution in different growth stages of the pyrite grains. To determine the trace element contents, the relative sensitivity factors of trace elements were determined using the data of EPMA and NanoSIMS in the enriched layers. Finally, the accuracy and precision of sulfur isotope analysis were evaluated by using the standard samples of pyrite.

4.1 Secondary ion imaging of trace elements

Pyrite grains from the Carlin-type ore in Lannigou were imaged with a high lateral resolution of ~250 nm in this study. The zoning layers with a width ranging from sub-micron to several microns were clearly shown in the secondary ion images (Fig. 4). The individual images were processed using the WinImage software (developed by CAMECA), including shift correction, accumulation, normalization by $^{34}S^-$ and line scan. The pyrite grain shows three types of zoning patterns, which indicate three different growing stages from the core to the rim. Stage 1 which is the core of the pyrite grain has very low concentration of Au and As, but relative high content of Se and Cu. Stage 2 is

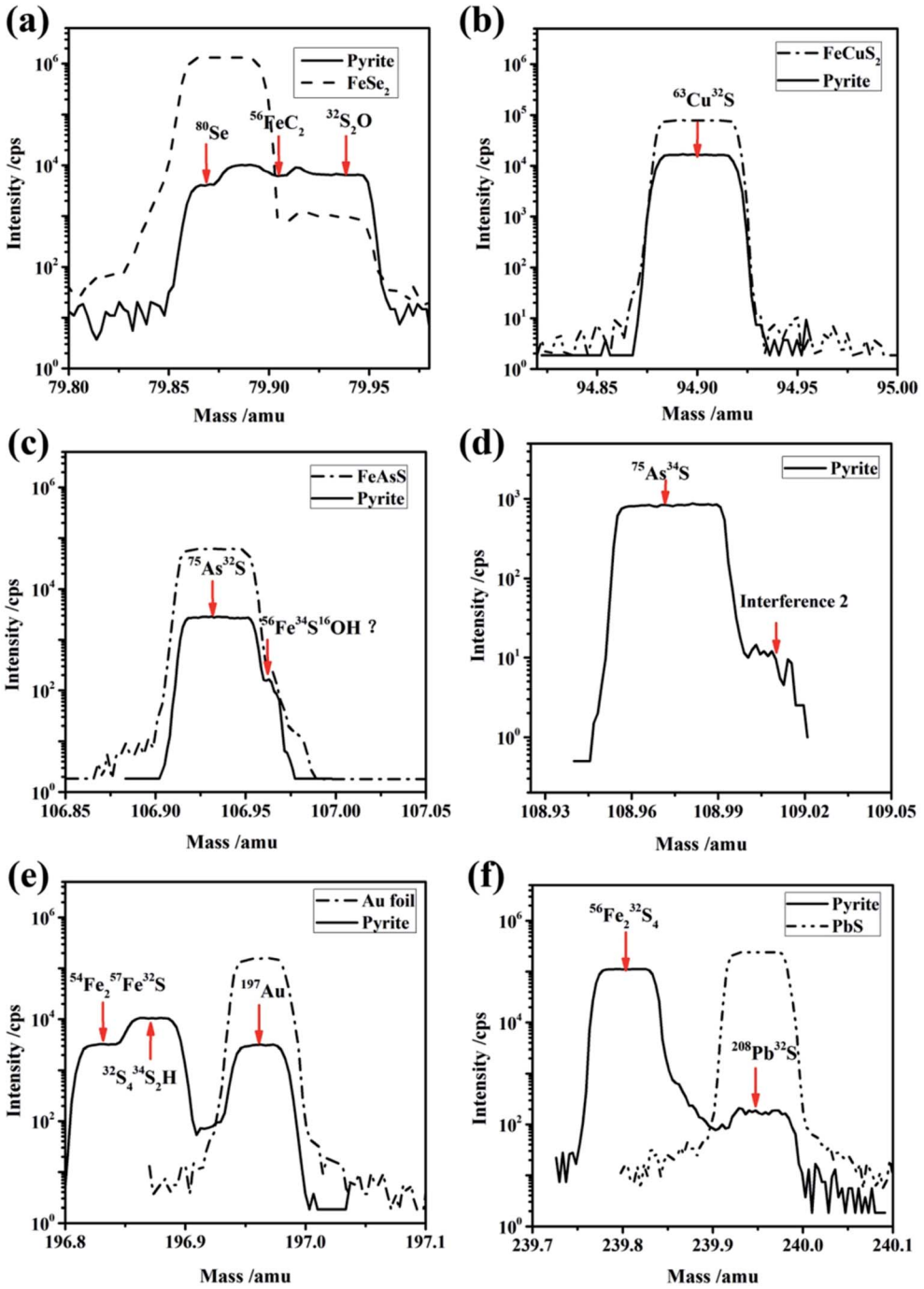

Fig. 2 The mass peak of the $^{80}Se^{-}$, $^{75}As^{32}S^{-}$, $^{63}Cu^{32}S^{-}$, $^{197}Au^{-}$ and $Pb^{32}S^{-}$ acquired in the pyrite sample and standard materials, including arsenopyrite, $FeSe_2$, Au foil and galena.

characterized by oscillatory zoning layers with the width of submicron order which is clearly shown in the image of $^{75}As^{32}S^{-}$ and $^{63}Cu^{32}S^{-}$. Stage 3 with the width of 5–7 μm in the rim of the grain is characterized by high concentration of Au and As and low concentration of Se. The hydrothermal fluid in stage 3 penetrated into the original pyrite through fractures in stages 1 and 2 (Fig. 4a and d). A cross profile with a length of ~40 μm was obtained along the line A–A′ with an accumulation window of 1 × 30 pixels (Fig. 4a) and the results are plotted in Fig. 5a. To study the paragenetic association of elements, correlations of different elements were checked through the three growth stages (Fig. 5b–d). There is a strong positive correlation between the distributions of $^{197}Au^{-}$ and $^{75}As^{32}S^{-}$ in stage 1 and stage 3, while the distribution of $^{75}As^{32}S^{-}$ was well consistent with that of $^{63}Cu^{32}S^{-}$ in stage 2 (Fig. 5a–d). This information could provide hints for the changing of chemical and thermodynamic conditions of the ore-forming fluid.

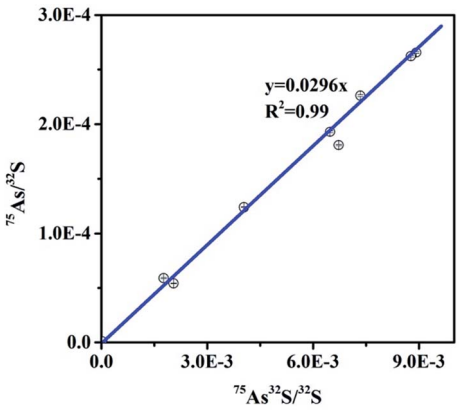

Fig. 3 The correlation between the ratios of $^{75}As^{32}S^{-}/^{32}S^{-}$ and $^{75}As^{-}/^{32}S^{-}$.

4.2 Relative sensitivity factors of the trace elements of pyrite

Relative sensitivity factors (RSFs) were required to determine quantitatively the contents of trace elements of minerals with SIMS. Normally, RSFs were determined by analyzing standard materials with known compositions. RSFs can be calculated by using the following equation:

$$\mathrm{RSF(A)} = \frac{C_{A^-}/C_{^{32}S^-}}{A^-/^{32}S^-} \quad (1)$$

where $A^-/^{32}S^-$ is the ratio of the secondary ion intensity of trace element A (A^-) to that of $^{32}S^-$. C_{A^-} and $C_{^{32}S^-}$ are the concentrations of A (A = As, CuS, Se, Au, PbS) and ^{32}S in the standard samples. In this study, the concentrations of A were determined by EPMA in the spot with a diameter of 2 μm, where A^- and $^{32}S^-$ had also been measured by NanoSIMS in image mode. Fig. 6 illustrates the way how we obtained trace element data by EPMA and NanoSIMS in the same spots. Secondary ion images of ^{34}S and trace elements were obtained by NanoSIMS. BSE images acquired by EPMA could be easily matched with secondary ion images (Fig. 6). Layers enriched with trace elements in the image were selected to determine the concentration of trace elements. All of the data are summarized in Table S1† and plotted in Fig. 7, showing linear relationships between the EPMA results and the relative intensity ratios acquired by NanoSIMS. These calibration curves can be used to calculate the trace elements with much lower concentrations than the detection limits of EPMA. The RSFs for As, CuS, Se, Au, and PbS were calculated to be 4.43 ± 0.28, 0.36 ± 0.04, 0.18 ± 0.03 and 38.0 ± 15.1, respectively. Au has a higher ion yield of Au^- than the other ion species under the Cs^+ bombarding. As shown in Fig. 6, the BSE image and As image match very well. The identification of analysis spots by EPMA and NanoSIMS could be easily achieved, according to the zoning layers and patterns. The deviation of data from the linear regression lines may mostly come from the analytical precision and accuracy of EPMA results. The low ion yield of $^{208}Pb^{32}S$

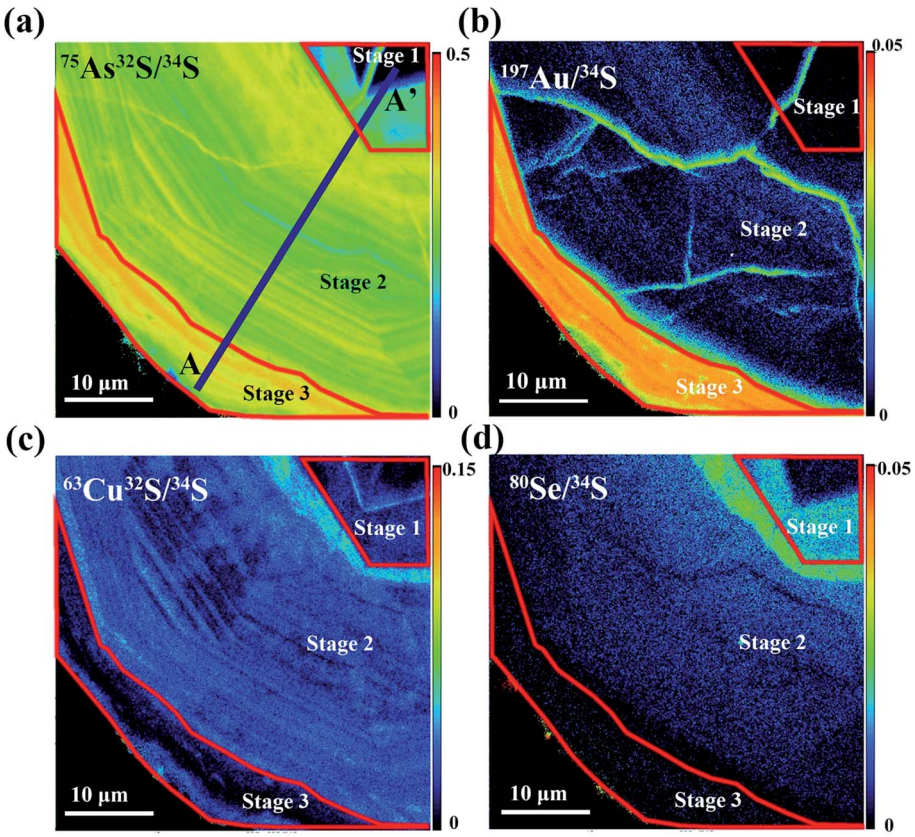

Fig. 4 Secondary ions of trace element distribution in pyrite from the Lannigou Carlin-type deposit. (a–d) Ion mapping normalized by $^{34}S^-$ for $^{75}As^{32}S^-$, $^{80}Se^-$, $^{63}Cu^{32}S^-$ and $^{197}Au^-$, respectively.

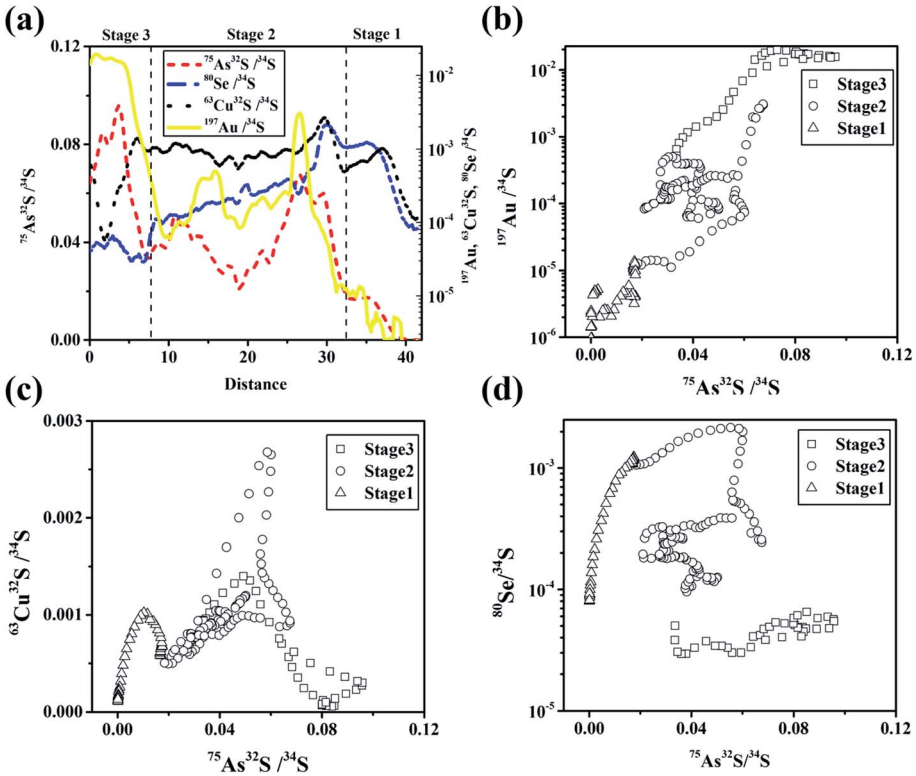

Fig. 5 A line profile of $^{75}As^{32}S^-$, $^{80}Se^-$, $^{63}Cu^{32}S^-$ and $^{197}Au^-$ along the red line in Fig. 4a and the concentration correlations between different elements in the three growth stages.

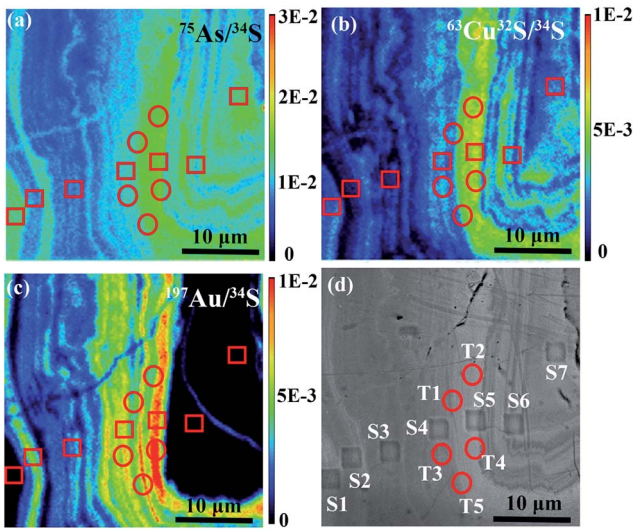

Fig. 6 (a–c) Ion image normalized by $^{34}S^-$ for ^{75}As, $^{63}Cu^{32}S^-$ and $^{197}Au^-$, respectively. (d) The backscattered electron image for the same area as the secondary ion image. □ with a size of 2 × 2 μm^2 in the image is the region for sulfur isotope analysis by NanoSIMS and ○ with a diameter of 2 μm in the image is for the trace element determination by EPMA.

caused a large error of the calibration curve for Pb content. Compared with the research of Barker *et al.* (2009), this work provided an approach to determine the RSFs of trace elements which could be used to quantify the trace element content.

4.3 Sulfur isotope measurements

Sulfur isotopes of ^{32}S and ^{34}S, together with trace elements, were counted with a Faraday cup (FC) and six electron multipliers (EMs), respectively. Because of the high counting rate of ^{34}S (~250 000 cps), the EM for ^{34}S could have a significant aging effect. As discussed by Zhang *et al.* (2014),[32] a higher voltage was applied on the EM for ^{34}S to make sure that the center of the pulse height distribution curve (PHD_{Max}) is about 300 mV to reduce the EM aging effect. The baseline of the Faraday cup was measured for 1 min before and after the analysis. After the deduction of the FC baseline, the intensity of $^{32}S^-$ was used to calculate the sulfur isotope ($^{34}S/^{32}S$). Table 1 summarizes the results of sulfur isotope analyses obtained in four different sessions. The analyses of the pyrite standards and references have uncertainties <0.5‰ (1SD) for $\delta^{34}S$. Using PY-1117 as the standard in all of the four sessions, the calibrated $\delta^{34}S_{VCDT}$ values of Balmat pyrite and the working references are consistent with the recommended value within an analytical uncertainty of ±0.5‰ (Fig. 8 and Table 1). Considering the same lateral resolution (1–2 μm) using NanoSIMS, the precision and accuracy in this work were consistent with those reported by Zhang *et al.* (2014),[32] but much higher than those reported in the other literature studies with a typical value of 2–3‰.[29,31,46] Williford *et al.* (2010) performed the sulfur isotope analysis with a comparable lateral resolution of 2 × 3 μm^2 and a higher accuracy of 0.4‰ (1SD) by using an IMS 1280. Combined with the measurement of trace elements, the method in this study

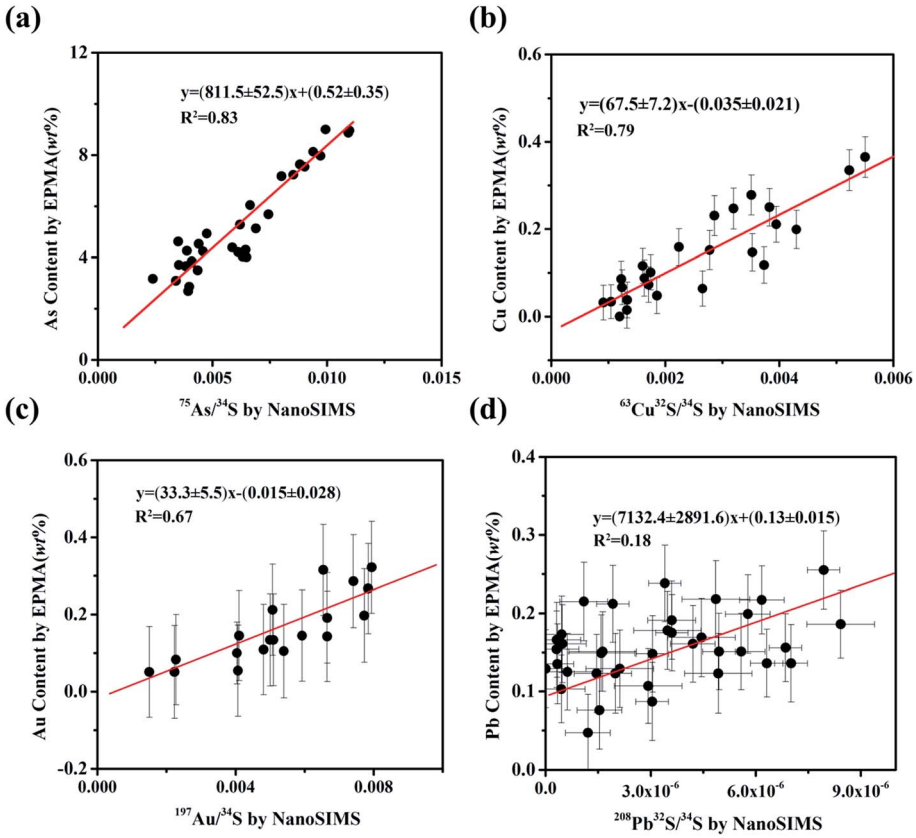

Fig. 7 (a–d) Calibration curve for the content determination of As, Cu, Au and Pb. The error bar for As (Fig. 6a) was within the symbols.

was aimed to analyze complexly zoned pyrite grains with thin layers (*e.g.* typical thin rims of pyrite in Carlin-type deposits).

Thereafter, we also analyzed the pyrite from Lannigou gold ore deposits and the results are shown in Fig. 9 and the ESI (Table S2†). The sulfur isotope ratios in the same layers varied within 1‰ and they varied by several per milles in different layers. Individual Pyrite grains can be divided into a core and rim. The core was formed in the pre-ore stage with low As and/or As-free, while the rim was formed in the ore stage with As and Au-rich. The fluctuation of As and Au concentrations and sulfur isotopes in the pyrite rim suggests fluid-mixing between two end-member ore fluids during mineralization. One of the ore fluids should be As and Au-rich with a lower $\delta^{34}S$ value, and the other one should be As-poor with higher $\delta^{34}S$.

4.4 Potential applications

In this study, pyrite in Carlin-type deposits was utilized to demonstrate the validity of the analytical methods. Besides the

Table 1 Sulfur isotope ratios of the pyrite standard samples measured in this study

Date	Sample	Mineral	n	$\delta^{34}S_{Raw}$	1SD	$\delta^{34}S_{Calib}$[a]	Bias[b]
2013-April	Balmat	Pyrite	12	9.2	0.2	16.4	0.3
	PY-1117	Pyrite	16	−7.0	0.3	—	—
	CS01	Pyrite	10	−2.8	0.4	4.2	−0.4
2013-July	Balmat	Pyrite	25	3.5	0.4	16.5	0.4
	PY-1117	Pyrite	17	−12.7	0.3	—	—
	CS01	Pyrite	10	−8.5	0.3	4.1	−0.5
2014-August	PY-1117	Pyrite	22	−1.4	0.4	—	—
	CS01	Pyrite	23	2.8	0.4	4.5	−0.1
2014-October	PY-1117	Pyrite	25	−5.6	0.4	—	—
	CS01	Pyrite	26	−1.8	0.4	4.1	−0.5

[a] The sulfur isotope calibrated with standard references: Balmat or 1117. [b] Bias is the difference between $\delta^{34}S_{Calib}$ and the recommended value.

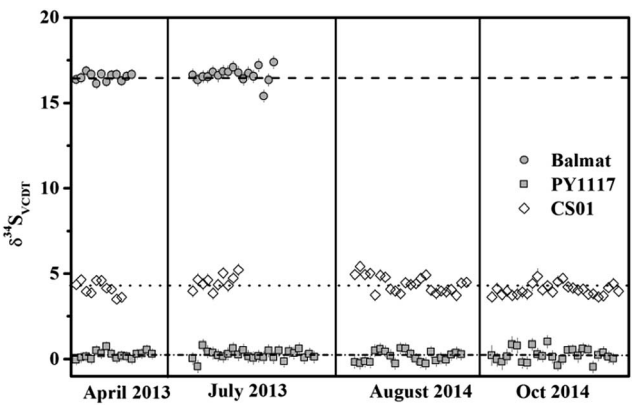

Fig. 8 Analytical reproducibilities of $\delta^{34}S_{VCDT}$ in pyrite standards and working references in four different sessions. The recommended values for the standards are shown by different horizontal lines. The error bars are shown with 1σ.

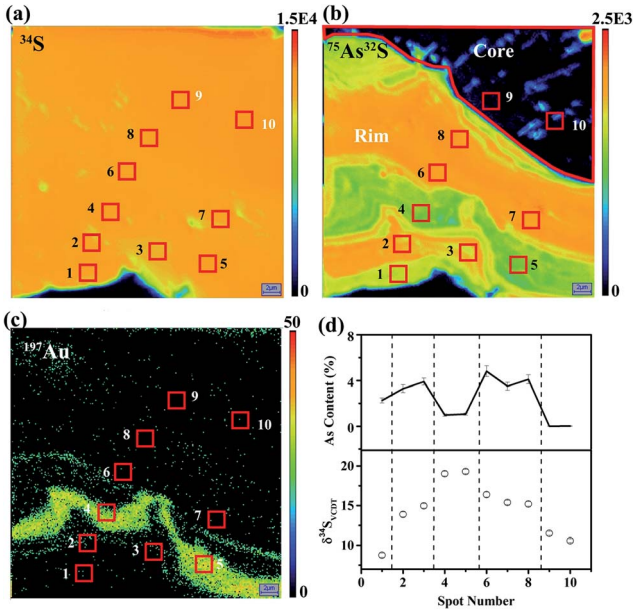

Fig. 9 Sulfur isotope and trace element analysis of pyrite from Lannigou Carlin type gold deposits. (a–c) Secondary ion images of ^{34}S, ^{75}As^{32}S and ^{197}Au; the red line in the ^{75}As^{32}S image was the boundary of the pyrite core and rim. (d) The sulfur isotope ratios and As contents in different layers.

trace elements of As, CuS, Se, Au and PbS, it is possible to try other trace elements (*i.e.* Zn, Ni, Ag, Pt, Tl,…), which are found in different types of pyrite. In this study, we utilized the same instrumental setup (slit configuration and intensity of primary ion current) to demonstrate that some metallogenic elements (Au, Pt, Ag, Ge, Ir, and Os) have higher ion yields under the sputtering of Cs^+ over O^-, (Table 2) which was consistent with

Table 2 Ion yields of metallogenic elements under Cs^+ sputtering and O^- sputtering

	Ion yield[a] (cps ppm^{-1} nA^{-1})	
Element	Yield with Cs	Yield with O
Pt	2.63×10^{1}	2.66×10^{-2}
Ir	2.23×10^{1}	1.61×10^{-1}
Os	4.07×10^{0}	1.56×10^{0}
Pd	7.56×10^{-1}	3.48×10^{0}
Rh	4.00×10^{-2}	9.60×10^{0}
Ru	6.54×10^{-1}	4.00×10^{1}
Ge	6.09×10^{0}	3.45×10^{0}
Cu	4.30×10^{0}	3.63×10^{0}
Ni	8.09×10^{0}	1.76×10^{0}
Au	2.54×10^{1}	2.50×10^{-2}
Se	2.70×10^{2}	
As	1.33×10^{1}	
CuS	1.34×10^{1}	
PbS	1.92×10^{-1}	

[a] Ion yield was calculated with the following equation: yield = counting rate/concentration/primary beam intensity. The measurement was done with pure metals.

that reported in the literature.[8,47] The other trace elements could also be measured with the ion species XS^- (X = Cu, Fe, Ni, As,…) in order to improve the sensitivities under the Cs^+ sputtering which provides a better lateral resolution than a Duoplasmatron oxygen ion source.[48] Trace element images obtained at the beginning of the analysis were an important tool to characterize different ore-stages and accurately determine the following sulfur isotope and trace element content. This method is aimed at the complex zoning layers of pyrite with the width ranging from 1 to 5 μm which are difficult to analyze with traditional methods. This method could also be applied for other sulfide minerals with very thin layers.

5. Conclusion

We carried out simultaneous analyses of S isotope ratios and trace elements of pyrite with a high lateral resolution using NanoSIMS. Secondary ions of $^{32}S^-$, $^{34}S^-$, $^{75}As^-$ ($^{75}As^{32}S^-$), $^{80}Se^-$, $^{63}Cu^{32}S^-$, $^{197}Au^-$ and $^{208}Pb^{32}S^-$ were simultaneously detected in the multi-collection mode with one Faraday cup (FC) and six electron multipliers (EMs). Relative sensitivity factors (RSFs) were vital to quantify the content of trace elements. To obtain the RSFs, layers enriched with trace elements were measured with EPMA and NanoSIMS 50L at exactly the same spot. The relative sensitivity factors (RSFs) for As, CuS, Au, and PbS were calculated to be 4.43 ± 0.28, 0.36 ± 0.04, 0.18 ± 0.03 and 38.0 ± 15.1, respectively.

To characterize the growth stages of the pyrite grain, sulfur and trace elements were first mapped with the size ranging from 20 × 20 to 40 × 40 μm^2 at a high lateral resolution of 250 nm. According to the secondary ion image, the spot analyses for sulfur isotopes ($^{34}S/^{32}S$) and trace elements were carried out with a FC for ^{32}S and EMs for other ion species at a high lateral resolution of ~2 × 2 μm^2. The accuracy and precision of sulfur isotope analysis were evaluated by using the standard samples of pyrite. The external reproducibilities (1SD) of sulfur isotopes were better than 0.5‰ and the analytical accuracy was better than 0.6‰. The reproducibilities of trace element measurements ranged from 10 to30% for Au, Cu, Pb and Se and less than 10% for As. This method has important potential applications in isotopic and elemental investigation of thin layers of pyrite and other sulfides with the width of 1–5 μm.

Conflicts of interest

There are no conflicts to declare.

Acknowledgements

The authors are grateful to Stephen J. Mojzsis for providing the Balmat and CAR 123 pyrite standards, and Mingjian Cao and Junxing Zhao for providing the working reference samples. This study was financially supported by the National Natural Science Foundation of China (41503012, 41273077, 41430105, and 41173075).

References

1 D. E. Canfield, *Am. J. Sci.*, 2004, **304**, 839–861.
2 J. Farquhar, H. M. Bao and M. Thiemens, *Science*, 2000, **289**, 756–758.
3 I. B. Butler, M. E. Bottcher, D. Rickard and A. Oldroyd, *Earth Planet. Sci. Lett.*, 2004, **228**, 495–509.
4 K. O. Konhauser, *Earth-Sci. Rev.*, 1998, **43**, 91–121.
5 D. E. Canfield, R. Raiswell and S. Bottrell, *Am. J. Sci.*, 1992, **292**, 659–683.
6 D. E. Crowe, J. W. Valley and K. L. Baker, *Geochim. Cosmochim. Acta*, 1990, **54**, 2075–2092.
7 R. R. Large, L. Danyushevsky, C. Hollit, V. Maslennikov, S. Meffre, S. Gilbert, S. Bull, R. Scott, P. Emsbo, H. Thomas, B. Singh and J. Foster, *Econ. Geol.*, 2009, **104**, 635–668.
8 S. L. L. Barker, K. A. Hickey, J. S. Cline, G. M. Dipple, M. R. Kilburn, J. R. Vaughan and A. A. Longo, *Econ. Geol.*, 2009, **104**, 897–904.
9 M. E. Fleet, S. L. Chryssoulis, P. J. Maclean, R. Davidson and C. G. Weisener, *Can. Mineral.*, 1993, **31**, 1–17.
10 P. Moller and G. Kersten, *Miner. Deposita*, 1994, **29**, 404–413.
11 X. W. Huang, J. F. Gao, L. Qi and M. F. Zhou, *Ore Geol. Rev.*, 2015, **65**, 900–916.
12 S. E. Gilbert, L. V. Danyushevsky, T. Rodemann, N. Shimizu, A. Gurenko, S. Meffre, H. Thomas, R. R. Large and D. Death, *J. Anal. At. Spectrom.*, 2014, **29**, 1042–1051.
13 B. Buhn, R. V. Santos, M. A. Dardenne and C. G. de Oliveira, *Chem. Geol.*, 2012, **312**, 163–176.
14 P. R. Craddock, O. J. Rouxel, L. A. Ball and W. Bach, *Chem. Geol.*, 2008, **253**, 102–113.
15 C. Bendall, Y. Lahaye, J. Fiebig, S. Weyer and G. P. Brey, *Appl. Geochem.*, 2006, **21**, 782–787.
16 E. H. Hauri, D. Papineau, J. Wang and F. Hillion, *Chem. Geol.*, 2016, **420**, 148–161.
17 M. J. Whitehouse, *Geostand. Geoanal. Res.*, 2013, **37**, 19–33.
18 J. Farquhar, J. Cliff, A. L. Zerkle, A. Kamyshny, S. W. Poulton, M. Claire, D. Adams and B. Harms, *Proc. Natl. Acad. Sci. U. S. A.*, 2013, **110**, 17638–17643.
19 R. Kozdon, N. T. Kita, J. M. Huberty, J. H. Fournelle, C. A. Johnson and J. W. Valley, *Chem. Geol.*, 2010, **275**, 243–253.
20 D. Papineau, S. J. Mojzsis, C. D. Coath, J. A. Karhu and K. D. McKeegan, *Geochim. Cosmochim. Acta*, 2005, **69**, 5033–5060.
21 S. J. Mojzsis, C. D. Coath, J. P. Greenwood, K. D. McKeegan and T. M. Harrison, *Geochim. Cosmochim. Acta*, 2003, **67**, 1635–1658.
22 R. L. Hervig, *Rapid Commun. Mass Spectrom.*, 2002, **16**, 1774–1778.
23 L. R. Riciputi, B. A. Paterson and R. L. Ripperdan, *Int. J. Mass Spectrom.*, 1998, **178**, 81–112.
24 K. H. Williford, M. J. Van Kranendonk, T. Ushikubo, R. Kozdon and J. W. Valley, *Geochim. Cosmochim. Acta*, 2011, **75**, 5686–5705.
25 E. S. Ingham, N. J. Cook, J. Cliff, C. L. Ciobanu and A. Huddleston, *Geochim. Cosmochim. Acta*, 2014, **125**, 440–465.
26 A. Pačevski, E. Libowitzky, P. Živković, R. Dimitrijević and L. Cvetković, *Can. Mineral.*, 2008, **46**, 249–261.
27 Z. Chang, R. R. Large and V. Maslennikov, *Geology*, 2008, **36**, 971–974.
28 K. E. Yamaguchi and H. Ohmoto, *Mem. Geol. Soc. Am.*, 2006, **198**, 143–156.
29 T. R. R. Bontognali, A. L. Sessions, A. C. Allwood, W. W. Fischer, J. P. Grotzinger, R. E. Summons and J. M. Eiler, *Proc. Natl. Acad. Sci. U. S. A.*, 2012, **109**, 15146–15151.
30 M. Kilburn and D. Wacey, in *Stromatolites: Interaction of Microbes with Sediments*, ed. V. Tewari and J. Seckbach, Springer, Netherlands, 2011, vol. 18, ch. 21, pp. 463–493.
31 M. Nishizawa, S. Maruyama, T. Urabe, N. Takahata and Y. Sano, *Rapid Commun. Mass Spectrom.*, 2010, **24**, 1397–1404.
32 J. Zhang, Y. Lin, W. Yang, W. Shen, J. Hao, S. Hu and M. Cao, *J. Anal. At. Spectrom.*, 2014, **29**, 1934–1943.
33 R. L. Hervig, F. K. Mazdab, P. Williams, Y. Guan, G. R. Huss and L. A. Leshin, *Chem. Geol.*, 2006, **227**, 83–99.
34 H. A. Storms, K. F. Brown and J. D. Stein, *Anal. Chem.*, 1977, **49**, 2023–2030.
35 W. Hsu, G. R. Huss and G. J. Wasserburg, *Geochim. Cosmochim. Acta*, 2000, **64**, 1133–1147.
36 D. E. Crowe and R. G. Vaughan, *Am. Mineral.*, 1996, **81**, 187–193.
37 T. Ushikubo, K. H. Williford, J. Farquhar, D. T. Johnston, M. J. Van Kranendonk and J. W. Valley, *Chem. Geol.*, 2014, **383**, 86–99.
38 B. Xiao, K. Qin, G. Li, J. Li, D. Xia, L. Chen and J. Zhao, *Resour. Geol.*, 2012, **62**, 4–18.
39 J. Zhao, K. Qin, G. Li, J. Li, B. Xiao and L. Chen, *Resour. Geol.*, 2012, **62**, 84–98.
40 B. R. Doe, *Geol. Soc. Am. Bull.*, 1962, **73**, 833–854.
41 M. H. Chen, Z. Zhang, M. Santosh, Y. Dang and W. Zhang, *J. Asian Earth Sci.*, 2015, **103**, 115–128.
42 M. H. Chen, L. L. Wu, P. J. Uttley, T. Norman, J. M. Zheng and Y. Z. Qin, *Acta Pet. Sin.*, 2007, **23**, 2423–2433.
43 X. C. Zhang, B. Spiro, C. Halls, C. J. Stanley and K. Y. Yang, *Int. Geol. Rev.*, 2003, **45**, 407–470.
44 C. Jones, D. A. Fike and P. Peres, *Rapid Commun. Mass Spectrom.*, 2017, **31**, 623–630.
45 G. Slodzian, F. Hillion, F. J. Stadermann and E. Zinner, *Appl. Surf. Sci.*, 2004, **231–232**, 874–877.
46 D. Wacey, N. McLoughlin, M. R. Kilburn, M. Saunders, J. B. Cliff, C. Kong, M. E. Barley and M. D. Brasier, *Proc. Natl. Acad. Sci. U. S. A.*, 2013, **110**, 8020–8024.
47 L. J. Cabri and G. Mcmahon, *Can. Mineral.*, 1995, **33**, 349–359.
48 J. Malherbe, F. Penen, M.-P. Isaure, J. Frank, G. Hause, D. Dobritzsch, E. Gontier, F. Horréard, F. Hillion and D. Schaumlöffel, *Anal. Chem.*, 2016, **88**, 7130–7136.